CIVIL ENGINEERING JOURNAL

Article no. 21

THE CIVIL ENGINEERING JOURNAL 3-2024

WIND TUNNEL TEST STUDY ON LATTICE HIGH SUPPORT OF BRIDGE IN TYPHOON AREAWIND TUNNEL TEST STUDY ON LATTICE HIGH SUPPORT OF BRIDGE IN TYPHOON AREA

Lijun Wan[1,2], Zehan Song[1], Quansheng Sun[1] and Shijie Wang[2]

1. *School of Civil Engineering and Transportation, Northeast Forestry University, Harbin, 150050, China; wlj2017@163.com;*
2. *Institute of Cold Regions Science and Engineering, Northeast Forestry University, Harbin 150040, China;*

ABSTRACT

At present, the typhoon stability of supports in typhoon areas is a key factor to ensure the safety of bridges. This paper analyzes the typhoon stability of lattice-type high supports by wind tunnel force measurement test and particle image velocimetry (PIV) test. The wind tunnel force test is used to obtain the static three-part force coefficient data of the lattice high-bracket under different flow fields and different wind angles. At the same time, the flow field visualization analysis of the horizontal plane flow field and vertical plane flow field of the high pier steel pipe stent model was carried out by using PIV technology. By quantitatively analyzing the vortex center vortex strength and turbulence degree of single-column and double-column brackets, the influence law of wind direction of wind field on the aerodynamic characteristics of lattice-type high-braced bracket was derived. It is shown that drag, lift and torque are the three main force effects that need to be fully considered in the calculation of wind resistance of the stent; when β=45°, the motion of the vortex is more intense, which leads to a corresponding increase in the aerodynamic mean and pulsation values of the model; the flow field of the steel pipe lattice-type stent has obvious three-dimensional characteristics, and therefore these characteristics should be fully considered in the numerical simulation. Lattice high-molded bracket has important practical significance in the construction of bridges in the typhoon area, which can improve the disaster-resistant capacity of bridges and reduce the construction cost; this paper provides reference opinions for the lattice high-molded bracket in the wind-resistant performance.

KEYWORDS

Typhoon area, Lattice high-bracket, Wind tunnel force test, Particle image velocimetry

INTRODUCTION

China's terrain is relatively complex, when the bridge is located in the coastal area, it is necessary to build long-span Bridges to ensure traffic operation [1]. As a bridge across the strait, the construction environment is mostly complicated, which has a great impact on the determination of the construction plan, and the construction technology of the main beam is more important [2]. The formwork support system of the main beam mainly includes fastening-type steel pipe scaffold, bowl-buckle steel pipe scaffold, portal scaffold and various types of steel brackets. Among them, the steel pipe lattice formwork support system has been recognized in the construction of two large-span Bridges in the Strait [3]. Lattice support structure has been gradually developed since the 1940s and has been widely used in recent years. This structure is mostly made of shaped steel, which is a tall

and flexible structure, characterized by light weight, small damping, and significant wind sensitivity [4]. Figure 1 shows the construction site of steel pipe column and Beret beam of Pingtan Large highway bridge.

Fig. 1 - Construction site of highway-railway bridge at Pingtan Straito of FuPing Railway

But so far, the research and summary of lattice stability is not systematic and cannot give effective help in engineering. Therefore, it has attracted the attention of many researchers at home and abroad. Jin et al. [5] studied the problems of cracking and excessive deformation in long-span lattice prestressed concrete box girder bridges, and found that the lattice grid model and the complete stress index system can more accurately simulate the actual load conditions and comprehensively evaluate the stress state of different plates of box girder. Jiang et al. [6] studied the creep damage behavior of lattice truss plate structures under high temperature environment and proposed a method to analyze the creep damage of lattice truss plate structures but did not put forward more suggestions on structural design optimization or performance improvement. Liu et al. [7] proposed a spatial frame lattice calculation model for structural analysis, which can effectively capture the complex behavior of the lattice, and found that the external prestressed tendons along the entire bridge and the vertical prestressed tendons inside the web can be used to reduce the principal stress in the web. Qiu et al. [8] studied the structural performance of lattice arch beams and proposed an optimization strategy for lattice arch beams: reduce the diameter of the main reinforcement bar and diagonal bar on the rock side, reduce the welding length, and cancel the stirrup. Sun et al. [9] studied the stability of the lattice steel pipe column support system, and concluded that the lattice steel pipe column support system could well adapt to the construction of high piers and large cross-border cast-in-place continuous box beams. Kim et al. [10] conducted an experimental analysis using material and structural testing to determine the performance of two steel lattice beams and found that underused steel members lead to a significant reduction in working loads.

Due to the "flexibility" of the steel pipe lattice formwork support system, the force is relatively complicated [11]. Especially under the action of wind load, the structure will produce certain movements, which in turn will cause wind pressure changes on the structure surface. These complex interactions make it difficult to accurately determine the size of the wind load on the structure [12]. In addition, with the increasing frequency of extreme weather around the world, bridge projects may be affected by wind loads during operation, resulting in adverse effects [13]. Due to structural problems, the wind resistance performance of lattice high supports is particularly significant. In order to explore the stress conditions and wind-induced effects of its structure under wind loads, aerodynamic analysis of the structure in the air flow field is required [14]. This paper mainly uses theoretical analysis [15], numerical analysis [16] and wind tunnel experiment [17] to analyze the wind dynamics of the lattice high support. In order to study the stability of support during bridge construction, wind tunnel force test of rigid model is used to evaluate the mechanical performance of lattice high support under static wind, and the influence of turbulence, the number of support, the number of support legs and the construction stage on high support is analyzed. The rigid model is analyzed by particle image velocimetry (PIV), and the vortex intensity and turbulence of vortex center are obtained by quantitative analysis. Finally, the influence law of high aerodynamic characteristics

is obtained. In view of the above problems, this paper carried out the research on the wind resistance of the lattice high support.

THREE-COMPONENT FORCE MODEL TEST OF LATTICE HIGH SUPPORT

Wind resistance performance is one of the key focuses in bridge design, and calculating the static force coefficients is crucial for assessing the static wind forces on structures. Obtaining static force coefficients can be achieved through three main methods: simplified formulae specified in standards, numerical simulations, and wind tunnel tests [18]. It directly influences the determination of the static wind stability of structures and provides the initial stable state for flutter and buffeting analysis.

Experimental condition

The test utilized the 25m long×4m wide×3m high closed-end return-flow rectangular cross-section wind tunnel, with the wind speed varying between in 3m/s to 50m/s, and the 3m long×0.8m wide×1.2m high small wind tunnel test section with wind speed varying between 1m/s and 23m/s. The laboratory is shown in Figure 2, and the test flow field mainly utilizes a three-dimensional pulsating anemometer to monitor the wind speed, and professional software is used for systematic measurement and analysis. Before the wind tunnel test, the monitoring instrument needs to be calibrated and processed to ensure the accuracy of the measurement data. The data testing and acquisition system utilizes a six-component high-frequency force balance, a data converter and an α-angle angle-of-attack change mechanism, etc. The measurement data of the test flow field includes a series of parameters such as wind speed, turbulence and wind speed profile.

Fig. 2 - Joint laboratory of wind tunnel and wave flume of Harbin Institute of Technology

Test conditions

This paper takes the new construction project of Pingtan Strait Road and Railway dual-purpose Bridge of Fuping Railway as the main research object. The bridge is located in the middle of Pingtan Strait, near the Pacific Ocean and 7.85km away from the mainland. The highway bridge part of Pingtan Large Bridge has five joints, and its layout is 4×40m continuous beam +4×40m continuous beam +6×40m continuous beam +5×40m continuous beam +4×32m continuous beam, with a total of 23 spans.

ABS plastic is used to make four kinds of lattice support design models by making model small parts splicing. Only the stiffness of steel is considered. ABS plastic has sufficient strength and stiffness, and no deformation occurs under the test wind speed and no obvious vibration phenomenon can ensure the measurement accuracy. The section D0#-D9# adopts a six-legged double-column support with a height of 52.380m and a cross-section of 27.120m×7.610m, while the section of a single support is 9.0m×7.610m. Section D9#-D19# adopts four-legged double-column support with a height of 61.702m and a section of 26.920m×7.610m, while the section of single support is 9.0m×7.610m. Considering the actual building and surrounding conditions, combined with the actual situation of the wind tunnel laboratory, the geometric scaling ratio of the model is determined to be 1:150. The model is geometrically similar to the physical building. As shown in Figure 3, the experimental model is D8 '#-D9' #, D10#-D11#, and D8#-D9#, respectively, the comparison scheme D8 '#-D9' #, and the model ratio is 1:150. The comparison scheme uses the

stent design scheme that the designer intends to adopt in the non-typhoon area, and a total of 9 working conditions. D8#-D9# lattice support corresponds to Case 1~3 working conditions; D8 '# lattice support corresponds to working condition No. 4; D9 '# lattice support corresponds to Case 5~6 working conditions; The highest support of D10#-D11# corresponds to the working condition of Case 7~9. Case 1, Case 4 and Case 7 are single scaffolds; Case 2 and Case 8 are double scaffolds; Case 5 refers to a single row of supports, while Case 3, Case 5 and Case 6 refer to cases where the main beams are poured but the supports are not removed.

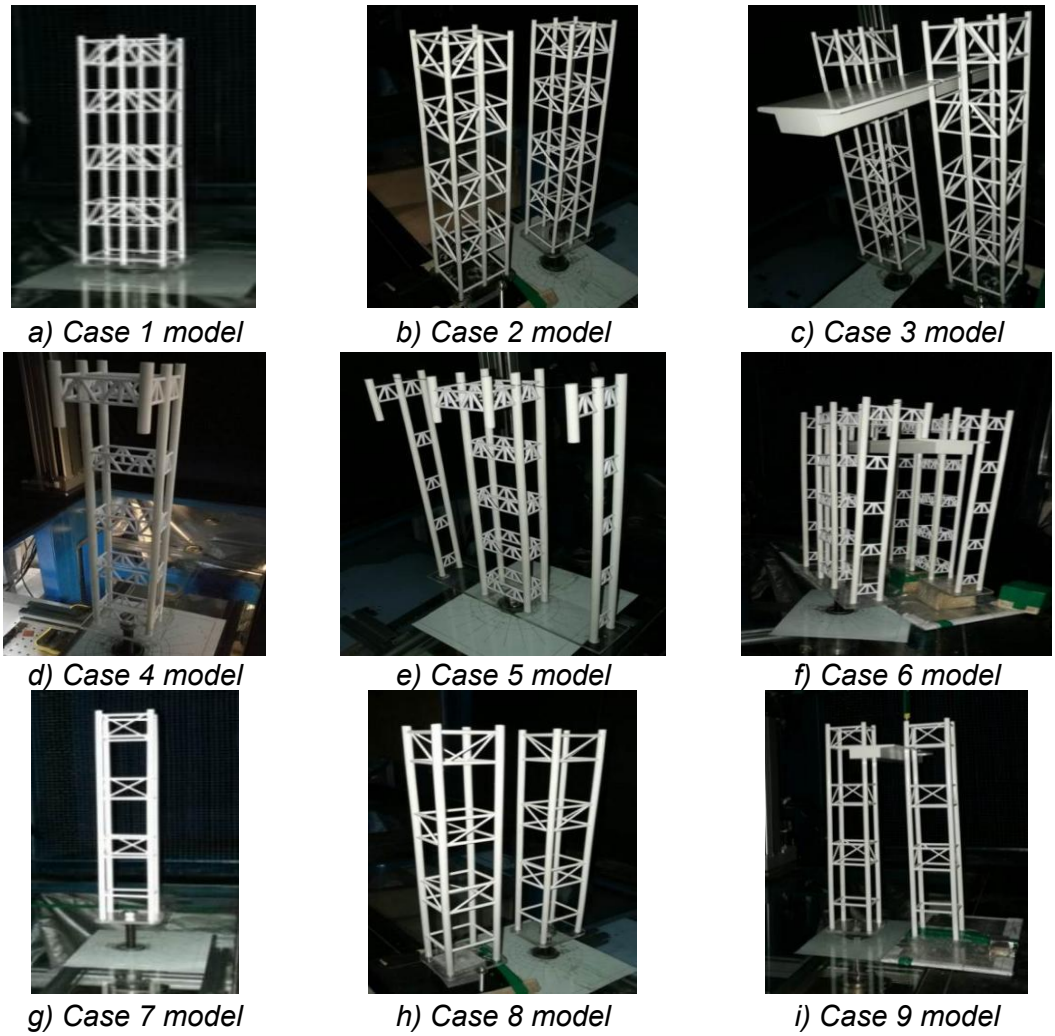

a) Case 1 model *b) Case 2 model* *c) Case 3 model*

d) Case 4 model *e) Case 5 model* *f) Case 6 model*

g) Case 7 model *h) Case 8 model* *i) Case 9 model*

Fig. 3 - Experimental pictures in wind tunnel

Wind field simulation

According to the building environment of a project and the structural loading code for buildings (GB50009-2012) issued by China, it can be determined that the type of geomorphology in which the project is located is class A geomorphology. According to the definition of Class A geomorphology, the geomorphological characteristics and meteorological conditions of the area are more consistent, which is suitable for the simulation test of the atmospheric boundary layer flow field. The model is scaled down according to 1:150, and three sharp splits and eight roughness are utilized in the wind tunnel to simulate the Class A wind field, as shown in Figure 4, and the wind speed and wind field turbulence profiles are shown in Fig 5. The wind speed of the wind tunnel test is 19 m/s. The sampling frequency of the force signal is 1000 Hz, the sampling time is 60 s, and the total length of the sampling samples of each measurement point is 60,000 data. Referring to the reference wind speed calculation method of our specification, the design reference wind speed of 10-year return

period in the design specification for wind resistance of highway bridges (JTGT D60-1-2004) is Vs10=35.0m/s, from which we can get the gradient wind speed of $V_d = V_{s10}(Z/10)^{\alpha}$, and the wind speed observed at the construction site is 45.4m/s. In summary, the design reference wind speed of V=45.4m/s is adopted.

Fig. 4 - Simulation of boundary layer turbulent wind field

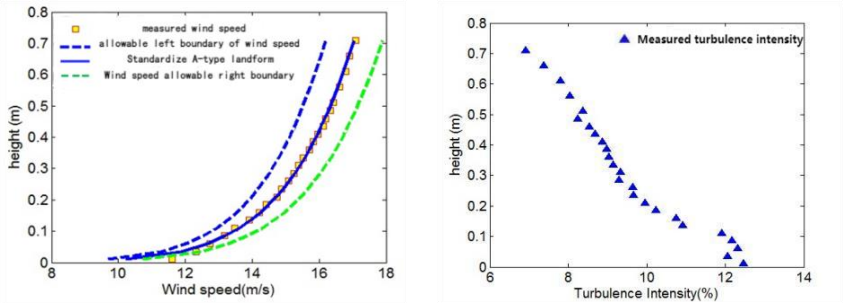

a) Wind speed profile *b) Wind field turbulence profile*

Fig. 5 - Parameter profiles of turbulent fields

PIV test scheme

Particle Image Velocimetry (PIV) first appeared in 1984 and is capable of capturing discrete particle images instead of difficult-to-observe particle scattering patterns [19]. This technique has very high measurement accuracy and resolution, can efficiently acquire transient images of the flow field, has powerful functionality, and is convenient and practical as it does not need to interfere with the object being measured.

Two laser beams, A and B, are emitted from a lens and then refracted by a lens inside the laser head to form a thin and bright laser surface that illuminates the flow field. The thickness of this laser surface is about 1mm or so. After being emitted, a CCD high-speed camera is utilized to expose and take pictures of the flow field, respectively, and a pair of images taken consecutively by the high-speed camera at the moments of t0 and t0+△t, respectively, as shown in Figure 6, where a pair of pictures is taken by using the PIV system, and a mutual correlation calculation is carried out by comparing the two pictures of the particle microclusters, and by identifying the change of the position of the particle microclusters (△x, △y) we can get the instantaneous By recognizing the position change (△x, △y) of the particle cluster, we can get the instantaneous velocity (u, v) of the particle cluster at that moment, and by taking consecutive pictures, we can get the flow velocity at different moments at the laser surface, and then we can get the velocity vector distribution of the whole two-dimensional flow field as shown in Figure 7. According to the velocity field results, it can be concluded that the quality of the velocity field obtained in this experiment is good, i.e., there are few bad points in the velocity field.

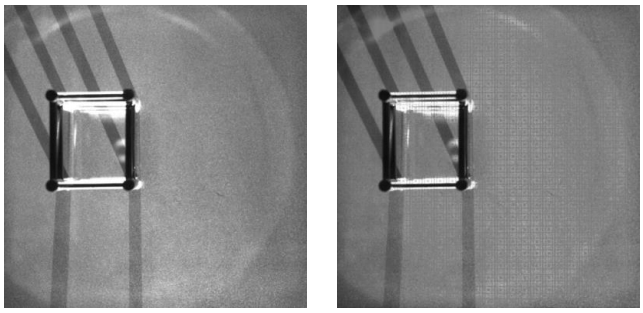

a) t_0 time *b) $t_0+\triangle t$ time*

Fig. 6 - Flow field image

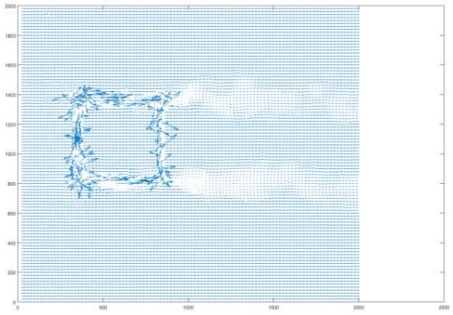

Fig. 7 - Velocity vector distribution

Using Particle Image Velocimetry (PIV) technology, visual flow field analysis was conducted on the six-legged single-pier, four-legged single-pier, six-legged double-pier, and four-legged double-pier models. For the double-pier support, flow field testing was exclusively performed on the downstream side support, specifically at the position of the downstream side support. Each model was tested in three horizontal planes and one vertical plane, with the cross-sectional positions shown in Figure 8. The experimental wind speed was 8m/s, and the incident wind deflection angles β were 0°, 45°, and 90°, as illustrated in Figure 9.

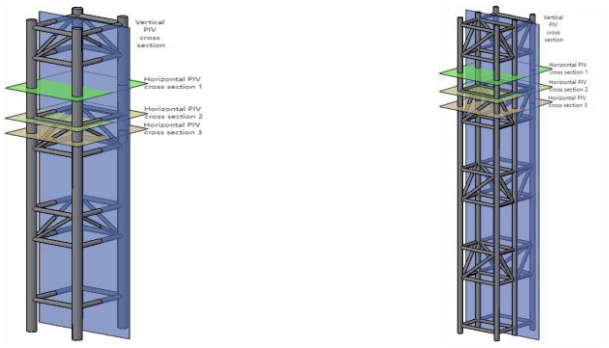

a) Four-legged bracket *b) Six-legged bracket*

Fig 8 - Sketch of cross sections in flow field

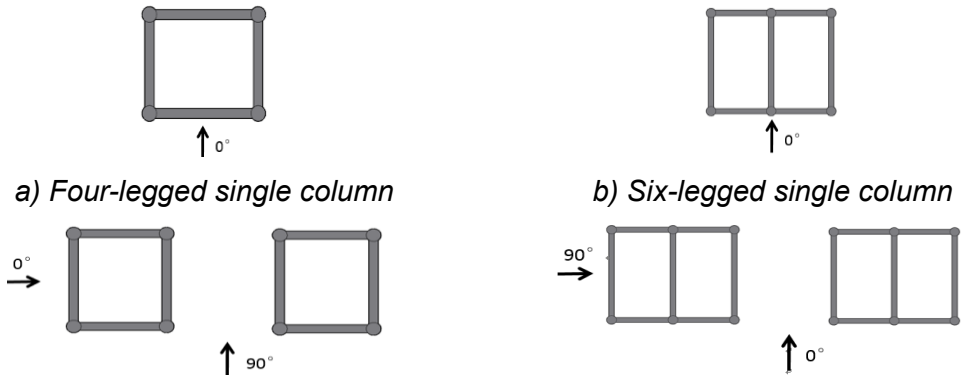

a) Four-legged single column *b) Six-legged single column*

c) Four-legged double columns *d) Six-legged double column*

Fig. 9 - Schematic diagram of yaw angle

EXPERIMENTAL ANALYSIS

Static three-force analysis coefficient

The static three-component force acting on the structural section is different according to the selected coordinate system. There are two representation methods, namely, according to the body axis coordinate system (the coordinate system is established along the main axis of the section center) and according to the wind axis coordinate system (the coordinate system is established along the wind direction), as shown in Figure 10.

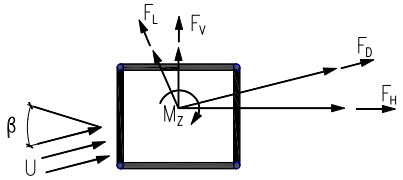

Fig. 10 - Sketch of three dimension static component force

The static trisection coefficient in the body axis coordinate:

$$C_H(\beta)=\frac{F_H(\beta)}{(0.5\rho U^2 HL)} \quad C_V(\beta)=\frac{F_V(\beta)}{(0.5\rho U^2 BL)} \quad C_M(\beta)=\frac{M_Z(\beta)}{(0.5\rho U^2 B^2 L)} \qquad (1)$$

U is wind speed，ρ is air density，β is incidence angle，$1/2\rho U^2$ is air flow dynamic pressure，H, B and L are the height, width and length of the main beam respectively，$F_H(\beta)$、$F_V(\beta)$ and $M_Z(\beta)$ are resistance, lift and torque under the action of shaft.

The static trisection coefficient in the wind axis coordinate:

$$C_D(\beta)=\frac{F_D(\beta)}{(0.5\rho U^2 HL)} \quad C_L(\beta)=\frac{F_L(\beta)}{(0.5\rho U^2 BL)} \quad C_M(\beta)=\frac{M_Z(\beta)}{(0.5\rho U^2 B^2 L)} \qquad (2)$$

$F_D(\beta)$、$F_L(\beta)$、$M_Z(\beta)$is the resistance, lift and torque under the action of the wind shaft.

（**1**）The flow field has the greatest influence on the static three-component coefficient of the D8 ' # and D9 ' # models (Figure 12), followed by the D8 # -D9 # model (Figure 11), and the D10 # -D11 # model (Figure 13). For D8 # -D9 # models, turbulence can reduce the absolute value of drag

coefficient. Case3 in the uniform flow field is significantly smaller than that in the turbulent flow field, and Case1~2 is the opposite. Case4and in the uniform flow field is greater than that in the turbulent flow field, and Case5is the opposite. Case 7 ~ 9 and are little affected by the flow field. The influence of flow field on torque coefficient has no obvious rule.

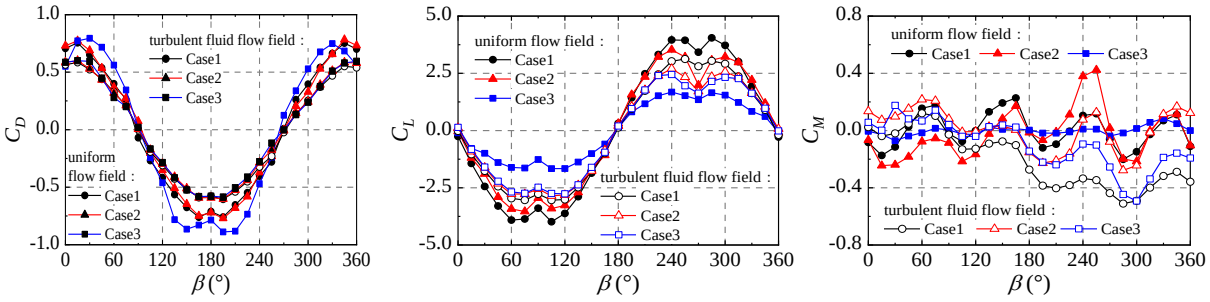

Fig. 11 - The aerodynamic force coefficients for Case1~3

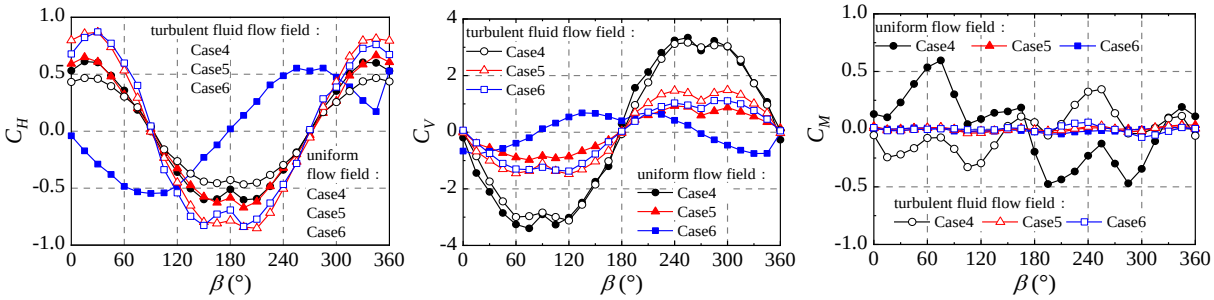

Fig. 12 - The aerodynamic force coefficients for Case4~6

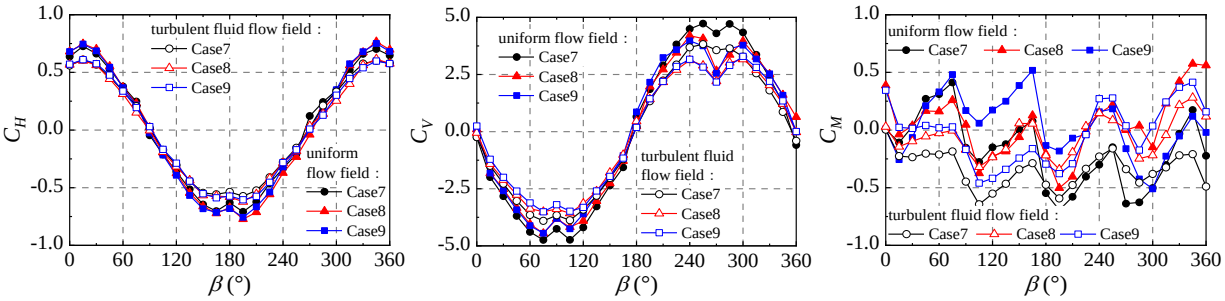

Fig. 13 - The aerodynamic force coefficients for Case7~9

（**2**）In the uniform flow field, compared with Case2 and Case3, it can be seen that due to the influence of the main beam, $|C_H|$ increases, $|C_V|$ and $|C_M|$ decrease ; comparing Case1 and Case2, it can be seen that the difference between the static three-component coefficients of single and double supports is small. Comparing Case5 and Case6, it can be seen that due to the influence of the main beam, the change trend of C_H with the wind deflection angle changes significantly, and $|C_V|$ decreases.

In summary, the influence of resistance, lift and torque should be fully considered in the wind resistance calculation of the support, and the influence of static wind load from different directions should also be considered. In the calculation of static wind, it is also necessary to consider the influence of wind angle, turbulence of flow field and construction stage on the support.

Characteristics of flow field around horizontal plane

Vorticity

The rotation of fluid micro-clusters is usually described by vorticity and vortex intensity. The vorticity represents the intensity of the rotation of the fluid micro-mass per unit area, and the vortex intensity represents the intensity of the vortex in the flow field. Both vorticity and vortex intensity can be used to identify the vortex core, that is, the region with the strongest rotation in the flow field, which usually corresponds to the region where turbulence occurs [20].

（1）Four-legged single column

Firstly, the flow field of the single-column model is visualized, as shown in Figure 14~16, which is the result of the vortex intensity of the three measured sections of the four-legged single-column model. From the results of the flow around a four-legged single column, it can be seen that the vortex intensity is small when the two rods are in the same direction as the incoming wind before and after β=0° and β=90°.When β=45°, the vorticity of the column wake is larger. Among them, the vortex intensity at the 0° wind angle is slightly larger than that at the 90° wind angle, indicating that the farther the distance of the column along the wind direction, the smaller the vortex intensity. The wake of each column forms an asymmetric vortex, and the vortex of the upper and lower columns interferes with each other.

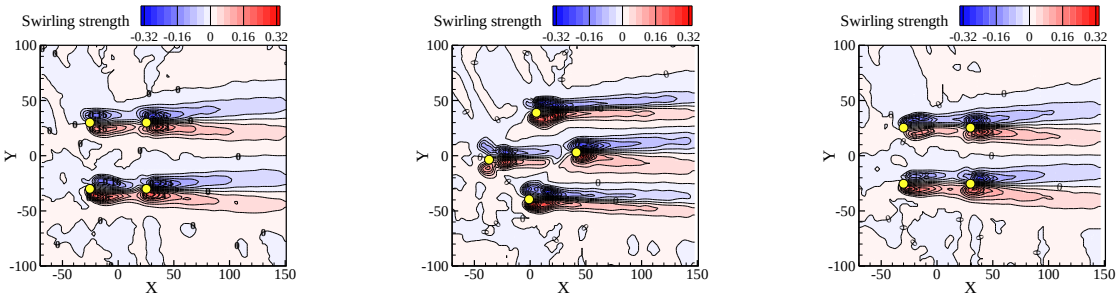

a) β=0° *b) β=45°* *c) β=90°*

Fig. 14 - Vortex strength diagram of section 1 of four columns model

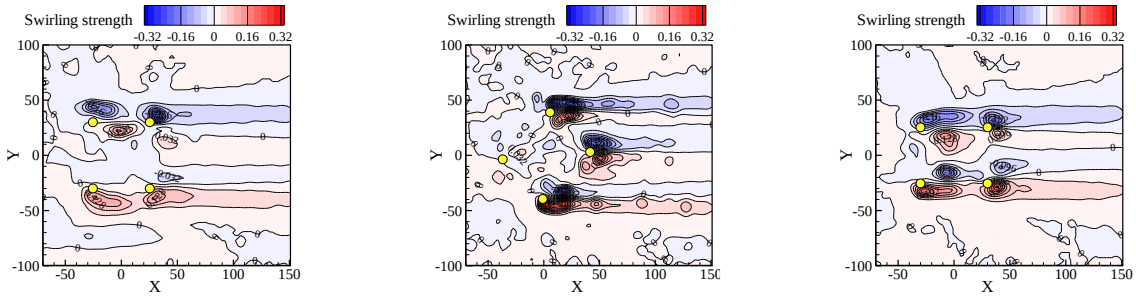

a) β=0° *b) β=45°* *c) β=90°*

Fig. 15 - Vortex strength diagram of section 2 of four columns model

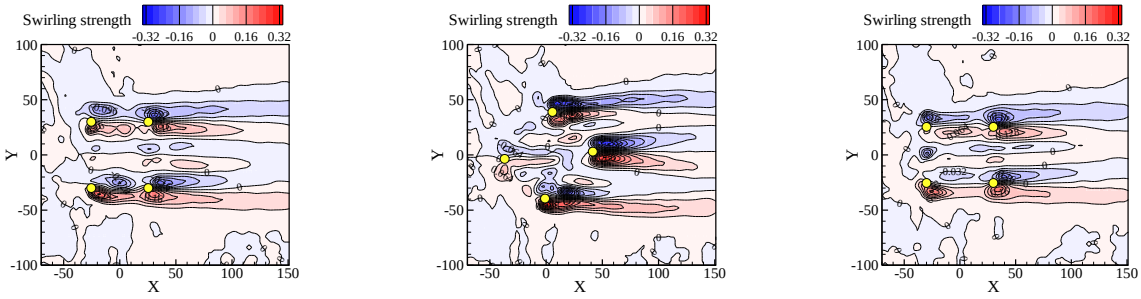

a) β=0° *b) β=45°* *c) β=90°*

Fig. 16 - Vortex strength diagram of section 3 of four columns model

（2）Six-legged single column

The flow field results of the six-legged single-column model are shown in Figures 17~19. Compared with the four-legged single-column, the flow field of the six-legged single-column is more different, that is, the flow field of the six-legged single-column has a stronger three-dimensional effect.

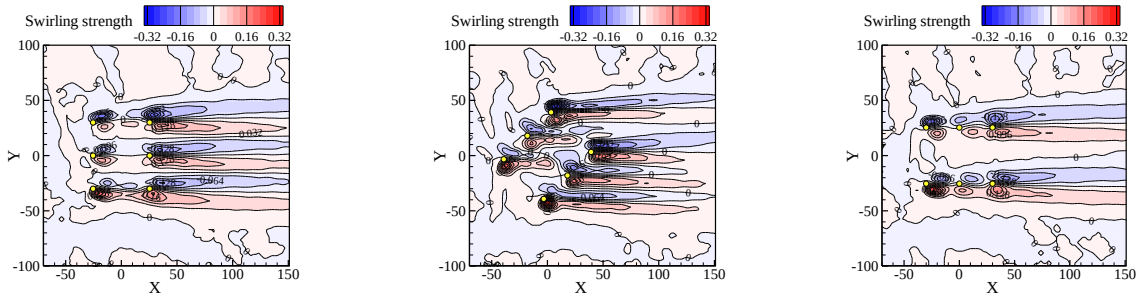

a) β=0° *b) β=45°* *c) β=90°*

Fig. 17 - Vortex strength diagram of section 1 of six columns model

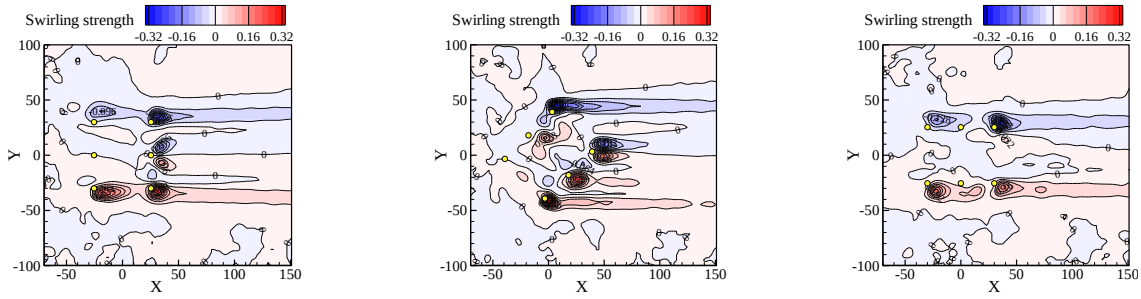

a) β=0° *b) β=45°* *c) β=90°*

Fig. 18 - Vortex strength diagram of section 2 of six columns model

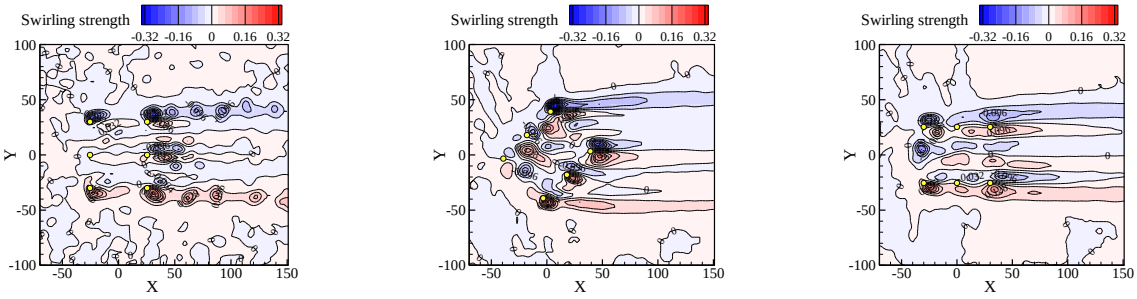

a) β=0° *b) β=45°* *c) β=90°*

Fig. 19 - Vortex strength diagram of section 3 of six columns model

（3）Four-legged double column

The vortex strength results of the four-legged two-column model are shown in Figures 20~22.Only the wind direction angles of 45° and 90° are measured. When β=45°, because the downstream support is less affected by the upstream support, the vortex strength at the tail of the downstream support of the double support is basically equal to that of the single column. When β=90°, due to the interference of the upstream support, the vortex intensity at the tail of the middle and downstream support of the double support is slightly smaller than that of the single support. Due to the influence of the upstream support, the vortex length and strength of the downstream support decrease significantly when β=90°.

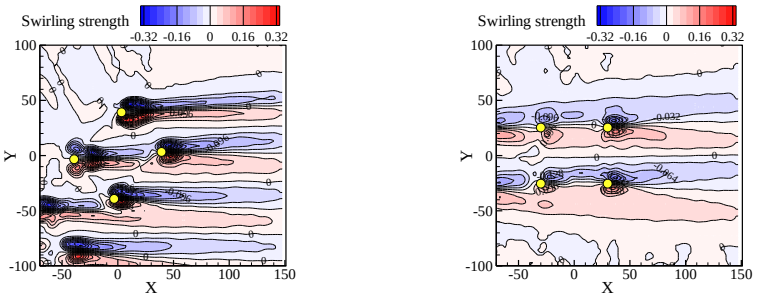

a) β=45° *b) β=90°*

Fig. 20 - Vortex strength diagram of section 1 of four columns model

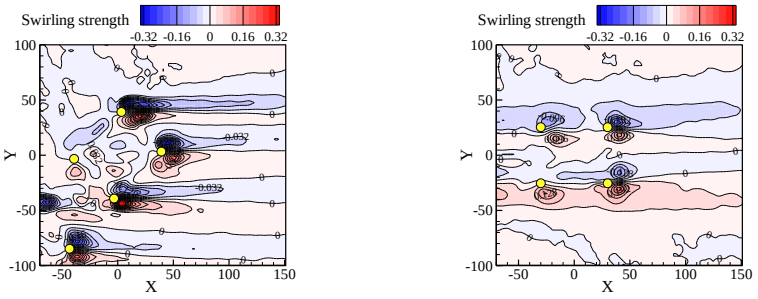

a) β=45° *b) β=90°*

Fig. 21 - Vortex strength diagram of section 2 of four columns model

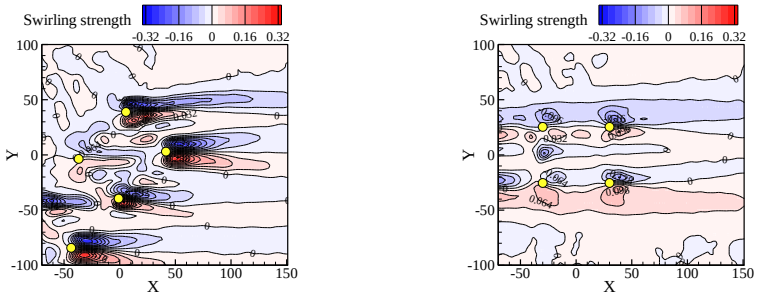

a) β=45° *b) β=90°*

Fig. 22 - Vortex strength diagram of section 3 of four columns model

（4）Six legs double column

The results of the vortex strength of the six-legged double-column model are shown in Figures 24~26. Compared with the single-column model, the vortex intensity of the downstream bracket is generally reduced when the double brackets coexist. Due to the interference of the upstream side support, the vortex length and strength of the β=0° condition are significantly smaller than those of the β=45° condition. The vortex center line of the column leg at the same height is the same under the condition of β=0°, so the front and rear interference is stronger than that under the condition of β=45°. The vortex length of section 1 is significantly longer than that of section 2 and section 3.

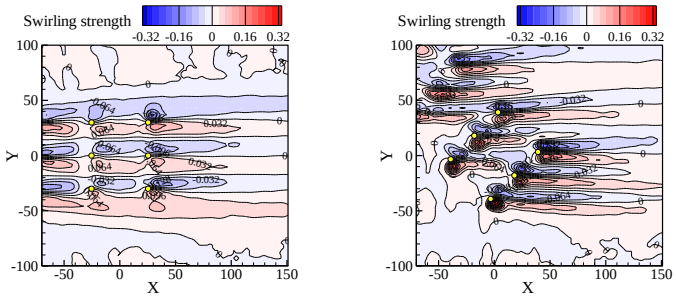

a) β=0° *b) β=45°*

Fig. 24 - Vortex strength diagram of section 1 of six columns model

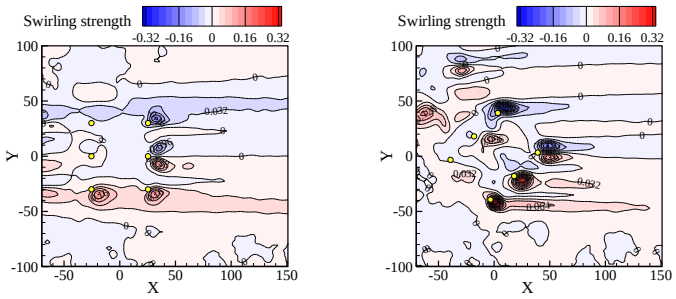

a) β=0° *b) β=45°*

Fig. 25 - Vortex strength diagram of section 2 of six columns model

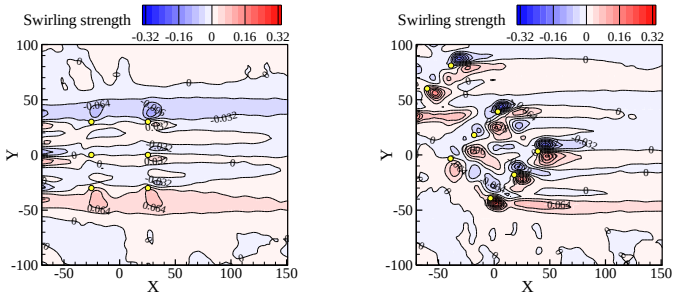

a) β=45° *b) β=45°*

Fig. 26 - Vortex strength diagram of section 3 of six columns model

Turbulent kinetic energy

The magnitude of the pulsation intensity of the flow field can be reflected by the standardized turbulent kinetic energy (T.K.E), which can be calculated by the following formula:

$$T.K.E = \frac{1}{2U_0}\left(u'^2 + v'^2 + w'^2\right) \qquad (3)$$

（1）Four-legged single column and six-legged single column

The normalized turbulent kinetic energy of the single-column model is shown in Figures 26~27. For the four-legged single-column model, the maximum turbulent kinetic energy is 0.025 at β=0°, 0.055 at β=45°, and 0.025 at β=90°.Therefore, it can be seen that the turbulent kinetic energy at β=45° is the largest. For the six-legged single-column model, the maximum turbulent kinetic energy is 0.011 at β=0°, 0.016 at β=45°, and 0.011 at β=90°, which is the same as the four-legged single-column model. The β=45° condition is the largest, but it is reduced by 60 %.

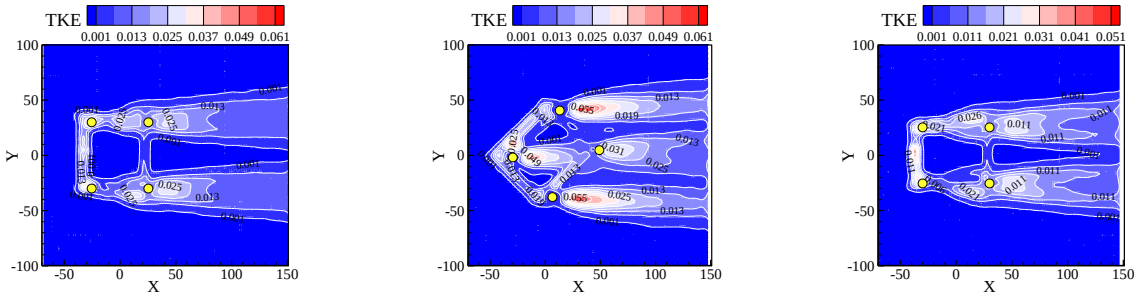

a) β=0° *b) β=45°* *c) β=90°*

Fig. 26 - Normalized turbulent kinetic energy diagram of the single bracket with four columns

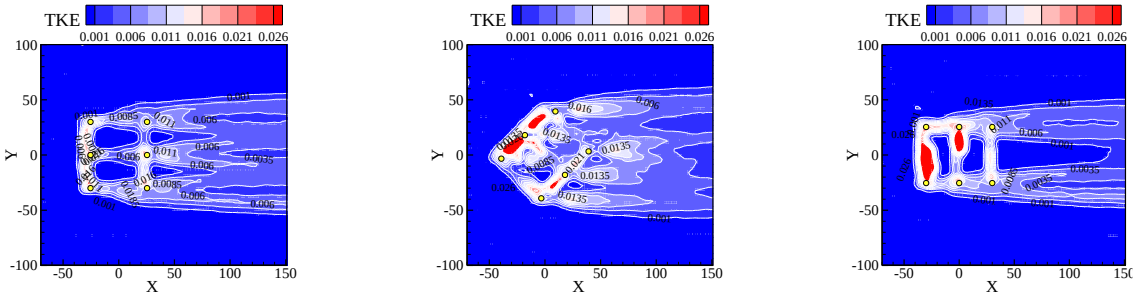

a) β=0° *b) β=45°* *c) β=90°*

Fig. 27 - Normalized turbulent kinetic energy diagram of the single bracket with six columns

（2）Four-legged double column and six-legged double column

The normalized turbulent kinetic energy of the two-column model is shown in Figures 28~29. For the four-leg two-column model, the maximum turbulent kinetic energy is 0.061 under the condition of β=45°, and the maximum is 0.025 under the condition of β=90°, which is more than two times smaller than the result under the condition of β=45°. For the six-legged double-column model, the maximum turbulent kinetic energy is 0.011 at β=0° and 0.0185 at β=45°.

a) β=45° *b) β=90°*

Fig. 28 - Normalized turbulent kinetic energy diagram of double brackets with four columns

a) β=0° *b) β=45°*

Fig. 29 - Standardized turbulent kinetic energy diagram of six-legged double-column model

Compared with the six-legged single-stent model, the maximum turbulent kinetic energy of the four-legged single-stent model increased by 56%, 71% and 57% at β=0°、45° and 90°, respectively. The maximum turbulent kinetic energy of the four-legged double-column model is 56 % and 70 % higher than that of the six-legged double-column model at β=45° and 90°, respectively. It shows that the aerodynamic force of the six-legged bracket model is much smaller than that of the four-legged bracket model at the same wind speed.

Characteristics of flow field around vertical plane

A vertical plane is selected to study the flow field results of the model, because the flow direction of the vertical plane passes through the longitudinal axis of the model. The flow fields of four-legged single-column, six-legged single-column, four-legged double-column and six-legged double-column models are shown in Figures 30~33, respectively. The maximum normalized turbulent kinetic energy of the vertical plane flow field of the model is about 0.12,0.04,0.01 and 0.0036, respectively. It shows that the six-legged bracket is the same as the above analysis results.

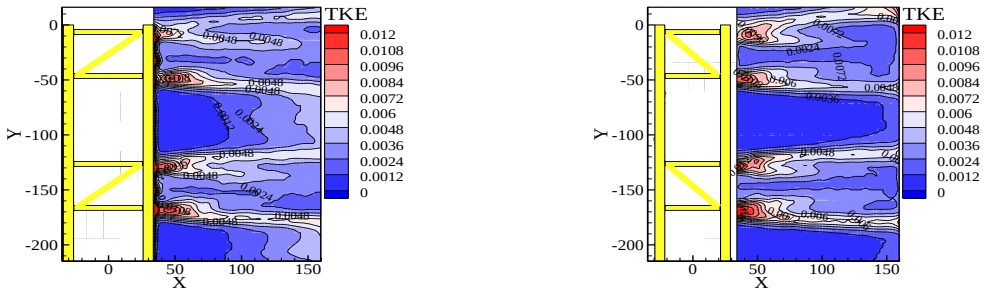

a) β=0° Turbulent kinetic energy diagram *b) β=90° Turbulent kinetic energy diagram*

Fig. 30 - Flow field results of single bracket with four columns

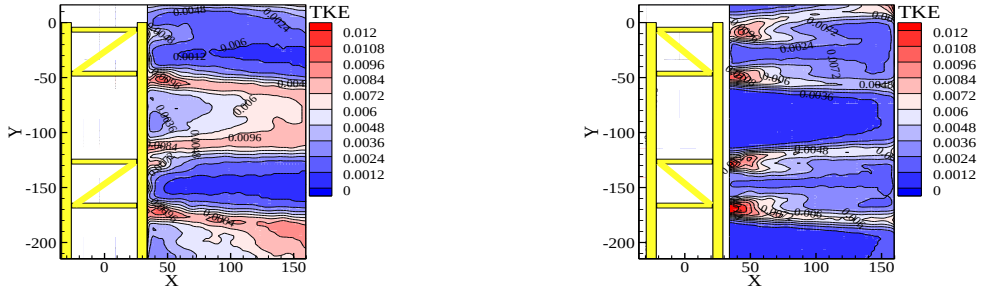

a) β=0° Turbulent kinetic energy diagram *b) β=90° Turbulent kinetic energy diagram*

Fig. 31 - Flow field results of double brackets with four columns

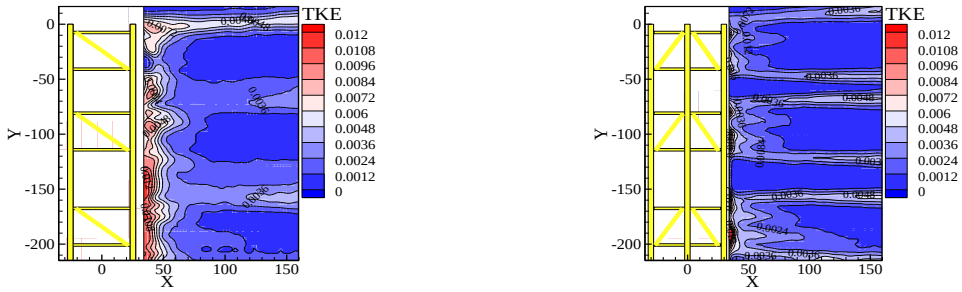

a) β=0° Turbulent kinetic energy diagram *b) β=90° Turbulent kinetic energy diagram*

Fig. 32 - Flow field results of single bracket with six columns

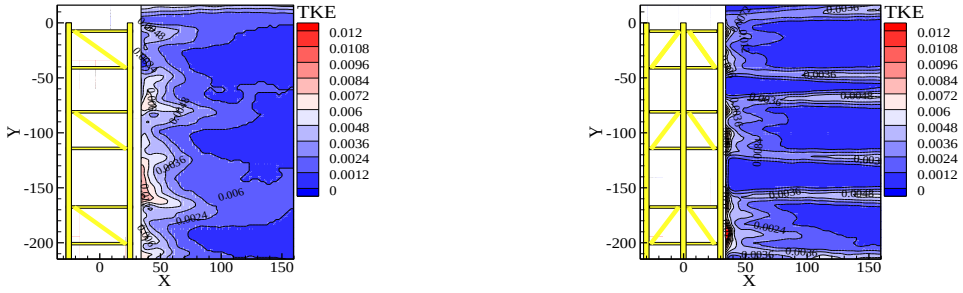

a) β=0° Turbulent kinetic energy diagram *b) β=90° Turbulent kinetic energy diagram*

Fig. 33 - Flow field results of double brackets with six columns

CONCLUSION

In this paper, the static wind force of lattice high support is studied by wind tunnel force test and PIV test, and the number of supports, flow field characteristics, construction stage and number of support legs are analyzed as variables. The following conclusions are obtained:

(1) Based on wind tunnel force test, the effects of flow field, wind Angle, number of supports and number of single support legs on static and aerodynamic characteristics of building supports are studied. For the first time, PIV technology is used to visualize the flow field of steel pipe support for high piers, and the influence of flow direction on the aerodynamic characteristics of steel pipe support for high piers is obtained. It can be applied to bridge construction, substation equipment and large industrial facility support structure using lattice high support, which provides reference for its wind resistance performance.

(2) Resistance, lift and torque are the three main effects that need to be fully considered when calculating the wind resistance of the support. In addition, the influence of wind yaw angle, turbulence of flow field and construction stage on wind should also be considered in the calculation of static wind.

(3) When β=0°and 90°, the vortex intensity and turbulent kinetic energy in the wake are smaller. In contrast, when β=45°, the motion of the vortex is more intense, which leads to a corresponding increase in the aerodynamic force and pulsation value of the model. At β=0°, 45° and 90°, the vortex intensity of section 2 is slightly larger than that of section 1 and section 3. Especially when β=45°, this difference is particularly obvious. In addition, the vortex intensity of the lower section 3 is smaller than that of the upper section 1. This shows that at the flat support, the vortex strength at the vortex core is the largest, and the vortex strength at the non-flat and diagonal support is greater than the vortex strength at the diagonal support.

(4) Compared with the four-legged single-column bracket, the maximum turbulent kinetic energy of the six-legged single-column bracket model in the wake field at β=0°, 45° and 90° is reduced by 56 %, 71 % and 57 %, respectively. In addition, the vortex intensity and turbulent kinetic energy at the vortex center of the six-leg support model are smaller than those of the four-leg support model.

(5) The flow field of steel pipe lattice support has obvious three-dimensional characteristics, so these characteristics should be fully considered in numerical simulation. In addition, there is obvious interference between the components, which requires accurate modeling and calculation in the simulation.

REFERENCES

[1] R. Hu, M. Yang, D. Meng, R. Cucuzza, M. Domaneschi, Robustness investigation of Horizontal Bidire ctional Hybrid Damping System applied to long-span bridges under near-fault pulse-like earthquakes, Soil Dy namics and Earthquake Engineering 184 (2024).

[2] D. Gao, Z. Deng, W. Yang, W. Chen, Review of the excitation mechanism and aerodynamic flow con trol of vortex-induced vibration of the main girder for long-span bridges: A vortex-dynamics approach, Journa l of Fluids and Structures 105 (2021).

[3] Y.-F. Yang, M. Liu, C. Hou, X.-M. Bie, Behaviour of four-legged square CFST latticed members unde r lateral cyclic loading, Journal of Constructional Steel Research 156 (2019) 54-74.

[4] T Jun, Key Technologies of construction of steel box girder lattice temporary piers and steel tower su pport frames [J] Sichuan Cement, (09) (2022) 201-202+213.

[5] Y. Jin, C. Sun, H. Liu, D. Xu, Analysis on the causes of cracking and excessive deflection of long spa n box girder bridges based on space frame lattice models, Structures 50 (2023) 464-481.

[6] W. Jiang, S. Li, Y. Luo, S. Xu, Creep Damage Analysis of a Lattice Truss Panel Structure, High Tem perature Materials and Processes 36(1) (2017) 89-96.

[7] C. Liu, D. Xu, L. Li, W. Cheng, Behavior of Concrete Segmental Box Girder Bridges with Open Webs , Journal of Bridge Engineering 20(8) (2015).

[8] W. Qiu, F. Lu, G. Wang, G. Huang, H. Zhang, Z. Zhang, C. Gong, Evaluation of mechanical perform ance and optimization design for lattice girders, Tunnelling and Underground Space Technology 87 (2019) 1 00-111.

[9] S Boyong, Zhu Guanghua, Wang Fengyuan, Stability study of cast-in-place box girder lattice steel pi pe column support system [J] Chongqing Architecture, 13(01) (2014) 50-52.

[10] H.J. Kim, K.I. Song, H.S. Jung, Y.W. Shin, J.H. Shin, Performance evaluation of lattice girder and sig nificance of quality control, Tunnelling and Underground Space Technology 82 (2018) 482-492.
[11] B.-Y. Deng, D. Tan, C.-L. Xia, G.-R. Liu, Y.-Q. Jiang, H.-Q. Xue, F. Qi, X.-W. Chen, L.-Z. Li, Experim ental study on flexural behavior of precast ultra-lightweight ECC plank with lattice girder at construction stage , Case Studies in Construction Materials 19 (2023).
[12] F. Li, L. Zou, J. Song, S. Liang, Y. Chen, Investigation of the spatial coherence function of wind loads on lattice frame structures, Journal of Wind Engineering and Industrial Aerodynamics 215 (2021).
[13] R. Zhou, Y. Ge, Q. Liu, Y. Yang, L. Zhang, Experimental and numerical studies of wind-resistance pe rformance of twin-box girder bridges with various grid plates, Thin-Walled Structures 166 (2021).
[14] X. Ji, G. Huang, Y.-G. Zhao, Probabilistic flutter analysis of bridge considering aerodynamic and stru ctural parameter uncertainties, Journal of Wind Engineering and Industrial Aerodynamics 201 (2020).
[15] S. Wang, F. Huseynov, M. Casero, E.J. Obrien, P. Fidler, D.P. McCrum, A novel bridge damage det ection method based on the equivalent influence lines – Theoretical basis and field validation, Mechanical Sy stems and Signal Processing 204 (2023).
[16] H. Jia, W. Wu, L. Xu, Y. Zhou, S. Zheng, C. Zhao, Numerical simulation and damaged analysis of a s imply-supported beam bridge crossing potential active fault, Engineering Structures 301 (2024).
[17] K. Li, Y. Han, C.S. Cai, Z. Qiu, A general modeling framework for large-amplitude 2DOF coupled non linear bridge flutter based on free vibration wind tunnel tests, Mechanical Systems and Signal Processing 22 2 (2025).
[18] W.-L. Chen, H. Li, H. Hu, An experimental study on a suction flow control method to reduce the unst eadiness of the wind loads acting on a circular cylinder, Experiments in Fluids 55(4) (2014).
[19] H. Mirzaeifar, K. Hatami, M.R. Abdi, Pullout testing and Particle Image Velocimetry (PIV) analysis of geogrid reinforcement embedded in granular drainage layers, Geotextiles and Geomembranes 50(6) (2022) 1083-1109.
[20] Y. Ran, W.-L. Chen, Y. Jin, H. Li, D. Gao, Reynolds number sensitivity of the vortex dynamics aroun d a long-span rail-cum-road bridge girder with three separated boxes, Journal of Wind Engineering and Indu strial Aerodynamics 250 (2024).